

A molecular dynamics study of the motion of a nanodroplet of pure liquid on a wetting gradient

Jonathan D. Halverson,^{1,a)} Charles Maldarelli,^{1,2} Alexander Couzis,¹ and Joel Koplik^{2,3}¹*Department of Chemical Engineering, City College of New York, New York, New York 10031, USA*²*The Benjamin Levich Institute for Physico-chemical Hydrodynamics, City College of New York, New York, New York 10031, USA*³*Department of Physics, City College of New York, New York, New York 10031, USA*

(Received 12 May 2008; accepted 16 September 2008; published online 29 October 2008)

The dynamic behavior of a nanodroplet of a pure liquid on a wetting gradient was studied using molecular dynamics simulation. The spontaneous motion of the droplet is induced by a force imbalance at the contact line. We considered a Lennard–Jones system as well as water on a self-assembled monolayer (SAM). The motion of the droplet for the Lennard–Jones case was found to be steady with a simple power law describing its center-of-mass position with time. The behavior of the water droplet was found to depend on the uniformity of the wetting gradient, which was composed of methyl- and hydroxyl-terminated alkanethiol chains on Au(111). When the gradient was nonuniform the droplet was found to become pinned at an intermediate position. However, a uniform gradient with the same overall strength was found to drive a droplet consisting of 2000 water molecules a distance of 25 nm or nearly ten times its initial base radius in tens of nanoseconds. A similar result was obtained for a droplet that was twice as large. Despite the many differences between the Lennard–Jones and water-SAM systems, the two show a similar overall behavior for the motion. Fair agreement was seen between the simulation results for the water droplet speed and the theoretical predictions. When the driving force was corrected for contact angle hysteresis, the agreement was seen to improve. © 2008 American Institute of Physics. [DOI: 10.1063/1.2996503]

I. INTRODUCTION

Pressure gradients or gravity are commonly used to drive liquids through pipes and tubes at human length scales, but the driving force required increases very rapidly when the size is reduced. Current interest in micro- and nanofluidic devices motivates research into alternatives. As illustrated in Fig. 1, one alternative for the transport of fluids at the nano-scale is a gradient in substrate surface energy, whereby intermolecular interactions draw the liquid molecules along the solid.

While gradient-driven flows have been observed in the laboratory by a number of groups and several approximate calculations have appeared, a number of open questions remain. For example, drop spreading phenomena often exhibit simple universal power laws for the long time behavior of drop position, shape, and contact angle,¹ but none has been established for the gradient case. Another important issue is that at the molecular level, a wettability gradient arises from discrete variations in molecular composition, which are not necessarily accurately modeled by a theorist's smooth variation of equilibrium contact angle with position. In particular, the effects of hysteresis and inhomogeneity may become an issue for very small drops. More generally, there are the questions of whether phenomena observed for millimeter or micron-sized drops persist at nanometer scales, and the rel-

evance of continuum modeling at the latter scale. Controlled atomistic simulations are an efficient means to investigate these issues, and in this paper we present molecular dynamics calculations, along with scaling arguments, which provide new insight into nanodroplet motion.

The motion of a liquid drop on a wetting gradient was first studied by Greenspan.² Later, the theoretical description was independently worked on by Brochard,³ who also considered motion due to a temperature gradient. Chaudhury and Whitesides⁴ were the first to realize the phenomenon in the laboratory. The gradient in this case was formed by following a procedure introduced by Elwing *et al.*⁵ where a silk thread saturated with decyltrichlorosilane is suspended in the vicinity of a silicon wafer. With the substrate tilted by 15° to the horizontal, it was shown that a 1–2 μl water droplet would migrate up the inclined solid against gravity with a velocity of 1–2 mm/s. Ford and Nadim⁶ provided a theoretical study of the motion of a cylindrical ridge of arbitrary

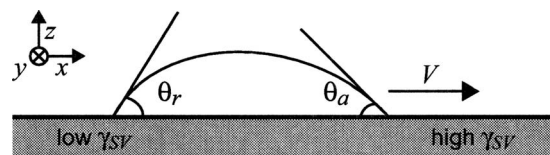


FIG. 1. Side view of a liquid drop on a wetting gradient with $\theta_a < \theta_r$, where θ_a and θ_r are the advancing and receding contact angles, respectively. On a surface where contact angle hysteresis is negligible a drop of any size will move in the direction of increasing γ_{SV} .

^{a)}Electronic mail: halverson@mpip-mainz.mpg.de.

shape due to a temperature gradient. Marangoni forces, which do not play a role in the motion of a drop on a wetting gradient, do become important when a thermal gradient is present. As experiments have shown, the droplet moves toward the cooler end of the gradient. In this work, we consider isothermal systems only.

Daniel *et al.* allowed droplets from saturated steam to condense on a radial wetting gradient.⁷ Small water droplets were found to migrate in the direction of increasing wettability with velocities that were two to three orders of magnitude larger than previously reported in Marangoni flows. When the steam was replaced with air, droplets 1–2 mm in size were found to give speeds of 2–3 mm/s, which is similar to previous findings.^{3,4,8}

Given sufficient time, a drop of any size will move on a wetting gradient. However, this is not observed for a surface that exhibits contact angle hysteresis. Experimentally, it has been shown that a drop must be greater than some critical size before it will move. Daniel and Chaudhury⁹ worked out an expression for the force due to contact angle hysteresis based on the work of Brochard.³ Their experiments with ethylene glycol on an alkylsilane substrate prepared in the same manner as previous experimental efforts showed that droplets no longer move when their base radius falls below a threshold value. It was demonstrated that in-plane vibration can help overcome the force due to hysteresis. Drop velocities increased from 1–2 to 5–10 mm/s when a speaker was attached to the substrate. The enhanced velocities due to in-plane vibration were examined further for five different liquids including water.¹⁰

Suda and Yamada¹¹ calculated the unbalanced Young force acting on the drop by extracting the advancing and receding contact angles from video frames. The same force was determined by a second method where a glass microneedle was inserted into the droplet and the force was related to the deflection of the needle. The two were found to be in good agreement. Based on their findings, a new expression for the hydrodynamic drag force was proposed.

Early works relied on the vapor-diffusion controlled procedure of Elwing *et al.*⁵ to prepare the wetting gradient. Later, Ito *et al.*¹² used photodegradation of an alkylsilane SAM to achieve the gradient. Gradients of different strengths were prepared by varying the intensity and time of photoirradiation. For the various gradient strengths considered, 2 μ l water droplets were found to migrate with average velocities of 1–7 mm/s. Photoirradiation was also used by Ichimura *et al.*⁸ on a photoisomerizable monolayer. This allowed for the direction and strength of the gradient to be changed reversibly. Contact angle hysteresis prevented water and other materials from moving on the gradient. Olive oil and liquid crystal systems were shown to traverse the gradient, however.

Subramanian *et al.*¹³ derived two expressions for the hydrodynamic drag force experienced by a spherical-cap droplet on a gradient of wettability. The first is based on a simplified result of Cox¹⁴ where it is assumed that the drop may be treated as a collection of wedges. The second uses lubrication theory while retaining the spherical-cap shape of the drop in the integration of the shear stress over the contact

area. The two expressions for the force give similar results for small contact angles and small values of the ratio of the slip length to base radius of the drop. These expressions were then used to describe the velocity of the drop which was compared to experimental data for tetraethylene glycol. In the experiments,¹⁵ droplets of several sizes were considered on the 1 cm gradient. The two expressions were found to overestimate the quasisteady velocity. When contact angle hysteresis was taken into account, the agreement was much better. This was the first experimental work to report results on the speed of the drop as a function of position along the gradient.

Aqueous droplets containing amphiphilic species may be driven on hydrophilic tracks embedded in a hydrophobic background by the covalent¹⁶ or noncovalent¹⁷ adsorption of the amphiphiles at the rear edge of the droplet. Here velocities of mm/s are observed on tracks that are typically a few millimeters wide. The noncovalent approach or reactive wetting has been studied by the lattice Boltzmann technique.¹⁸

Zhang and Han¹⁹ induced the motion of a pure fluid by using a strip of hydrophilic material of spatially uniform surface energy embedded in a background of hydrophobic material. The shape of the strip was tailored to optimize the speed of the spreading front. Using mica embedded in low-density polyethylene, the average spreading velocity was found to be 6.8 cm/s when the substrate was arranged horizontally.

In this work, the wetting gradients are generated on simulated atomic surfaces using molecular models of self-assembled monolayers (SAMs) with mixed terminal functionality. SAMs have received much attention in recent years because they are simple to prepare and provide well-ordered dense monolayers at full coverage, which allows for the control of surface properties.^{20–23} Alkanethiols on Au(111) are the most studied cases. The reported structure of such systems has changed many times over the years^{24–26} and is still being refined.²⁷ Recently, Riposan and Liu,²⁸ based on their scanning tunneling microscopy results and the computer simulation results of Li *et al.*,²⁹ have proposed a structural model for undecanethiol on Au(111). A modified version of this new model is used for the present study.

There have been a number of recent simulation studies of pure fluids on heterogeneous substrates. Adao *et al.*³⁰ looked at the spreading of a Lennard–Jones droplet on a regular square array of alternating solvophobic and solvophilic patches. Lundgren *et al.*³¹ examined a similar substrate pattern but with nanodroplets of water. Ultrahydrophobic surfaces were also investigated in this study. Dupuis and Yeomans³² conducted lattice Boltzmann simulations to study the wetting of patterned surfaces. Grest *et al.*³³ simulated the spreading of short chain polymer droplets on substrates with alternating strips of wetting and nonwetting materials. And Halverson *et al.*³⁴ studied the wetting behavior of water droplets on phase separated SAMs.

A. Theory

The driving force for the motion of a droplet on a wetting gradient is the unbalance of surface forces at the contact

line or the Young force. In this work, we consider either a highly distorted spherical droplet placed atop a wetting strip or a cylindrical-cap droplet whose shape is maintained by periodicity in the transverse direction. In the latter case, with reference to Fig. 1, the driving force in the x -direction per unit length in the y -direction is

$$F^{(y)} = \gamma [\cos \theta_e(x_a) - \cos \theta_e(x_r)], \quad (1)$$

where $\theta_e(x_a)$ and $\theta_e(x_r)$ are the equilibrium contact angles at the advancing and receding edges, respectively, and γ is the liquid-vapor interfacial tension. This expression ignores contact angle hysteresis.

The driving force is opposed by the hydrodynamic resistance acting on the fluid due to the solid substrate. This force has been derived using various simplifying assumptions and for different droplet geometries. For a ridge, Brochard³ using lubrication theory found an expression for the drag force in the x -direction per unit length in the y -direction [Eq. (21) of the original work]:

$$F^{(h)} = 6\mu \frac{V}{\theta_0} \ln \left(\frac{x_{\max}}{x_{\min}} \right), \quad (2)$$

where μ is the fluid viscosity, V is the velocity, x_{\max} is half the base radius of the ridge, and x_{\min} is a molecular size (which enters as a cutoff in the calculation). In Eq. (2), θ_0 is an average dynamic contact angle given by

$$2 \cos \theta_0 = \cos \theta_e(x_a) + \cos \theta_e(x_r). \quad (3)$$

Equations (1)–(3) lead to the quasisteady velocity of the drop. Inertial effects will be shown to be negligible.

II. SIMULATION METHODOLOGY

We consider two different cases involving droplet motion on a wetting gradient, first, a generic Lennard–Jones system with simple short-ranged interactions and, second, an aqueous system based on realistic interactions and experimentally realizable materials. The reason both simulations are presented here is that we observe strong similarities in their behavior, suggesting that our results have broad applicability beyond the particular materials and configuration considered here. The first case in addition involves a somewhat complicated drop configuration (and, in fact, was originally carried out for another purpose), while the geometry of the aqueous system allows us to focus cleanly on the effects of the wetting gradient.

A. Lennard–Jones system

The wetting gradient here is applied to a linear strip of wetting atoms extending down the middle of a nonwetting background on a periodic planar substrate. The substrate is a single layer of fcc unit cells (two atomic layers) of density $0.9\sigma^{-3}$ and dimensions $80.56\sigma \times 499.8\sigma$, and the wetting region is half as wide, and extends along the full length. A liquid drop of 16 704 molecules in the form of four-atom flexible chains is placed atop the wetting strip and allowed to move. All atoms interact via a Lennard–Jones potential,

$$U_{LJ}(r) = 4\epsilon \left[\left(\frac{r}{\sigma} \right)^{-12} - c_{ij} \left(\frac{r}{\sigma} \right)^{-6} \right], \quad (4)$$

with a cutoff at 2.5σ and shifted by a linear term adjusted so that the force vanishes at the cutoff. The coefficient c_{ij} varies the attractive interaction between atomic species i and j , and has the standard unit value for the fluid-fluid and solid-solid cases. The interaction between nonwetting solid and fluid has $c=0$, and for wetting solid and fluid c varies linearly between 0.75 and 2.0 along the length of the substrate. In addition, a finite extensible nonlinear elastic (FENE) interaction³⁵ acts between adjacent atoms in a chain to bind them into molecules. The motivation for a molecular rather than a monatomic liquid is to sharpen the liquid-vapor interface, which would be rather diffused in the latter case. The same molecular model has been used in an earlier study³⁶ of pearling instabilities in nanoscale flow on patterned surfaces.

In the simulations, the atoms composing the drop are initially placed on solid lattice sites within a rectangular box sitting atop the low- c end of the wetting strip, and the temperature is ramped up from $0.1\epsilon/k_B$ to $1.0\epsilon/k_B$ over a 500τ interval, using velocity rescaling. [Here, $\tau = \sigma(m/\epsilon)^{1/2}$, where m is the atomic mass, is the natural time unit for the simulations.] At this stage, the drop has melted into a rounded box shape. The temperature is subsequently fixed at 1.0 for the remainder of the simulation by a Nose–Hoover thermostat.

B. Water–SAM system

The wetting gradient is constructed using mixed monolayers with either methyl or hydroxyl termination. The monolayer is composed of 90 chains in the axial or x -direction and 8 chains in the transverse or y -direction. Two different gradients are considered and while both are composed of the same number of CH_3 - and HOCH_2 -terminated chains, one is more uniform than the other.

The structure of the chains is based on the model proposed by Riposan and Liu.²⁸ We adopt the model for phase B of their work where the monolayer forms a $(4\sqrt{3} \times 2\sqrt{3})R30^\circ$ lattice or $c(4 \times 2)$ superlattice. The sulfur atoms are located in the triple-hollow sites where they form a triangular lattice with a nearest-neighbor (NN) spacing of 4.97 Å. With reference to Fig. 2, each of the four chains per unit cell have the same tilt angle ($\theta=30^\circ$) and direction of

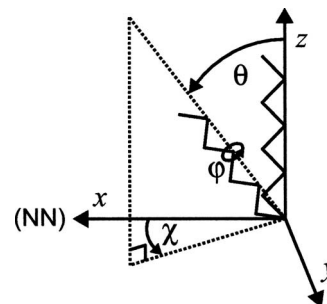


FIG. 2. The orientation of each chain in the monolayer is described by a tilt angle (θ), a direction of tilt (χ), and a twist angle about the molecular axis (ϕ). This diagram shows a methyl-terminated chain with its eight united atoms. The x -direction corresponds to a NN direction.

tilt ($\chi=15^\circ$). The individual twist angles are different. Further details of our SAM model and its predictions have been described in a previous study.³⁴

The wetting properties of SAMs composed of alkanethiols become independent of chain length when the number of methylene groups in the chain becomes large.^{37,38} Because of this, to reduce computation time, we only consider eight or ten atomic layers (depending on the terminal group of the chain) and ignore the remaining methylene groups, sulfur atoms, and gold lattice. Since the overall structure of pure SAMs composed of alkanethiols with either CH_3 or OH terminal groups has been shown to be similar,^{39,40} we assume that our model holds for both chains. Methyl and methylene groups are treated as united atoms while the oxygen and hydrogen atoms of the hydroxyl group are treated atomically. This means that methyl-terminated chains are composed of eight united atoms or $\text{CH}_3(\text{CH}_2)_7-$ while HOCH_2 -terminated chains or $\text{HOCH}_2(\text{CH}_2)_7-$ are composed of two explicit atoms and eight united atoms. The bottom two atomic layers of each chain are fixed throughout the simulation. This keeps the SAM in place and helps impose the proper structure on the chains. A one-dimensional wetting gradient is created by varying the surface concentration of hydroxyl-terminated chains in the x -direction. The hydroxyl surface concentration varies linearly with position over a distance of roughly 35 nm. The magnitude of the gradient is $1.4 \times 10^{-4} \text{ OH}/\text{\AA}$ or, based on our measurements of the water contact angle, an average of $3.2^\circ/\text{nm}$.

The motion of water droplets consisting of 2000 and 4000 molecules was examined on the two different wetting gradients. The droplets were constructed by extracting hemicylindrical shapes from a large simple cubic lattice of randomly orientated water molecules arranged at ambient liquid density. The hemicylindrical droplets were placed on the hydrophobic end of the wetting gradient at initialization. In this work, a surface is termed hydrophobic if the water contact angle is greater than 90° . Conjugate gradient energy minimization was performed for 10 000 steps. The molecular dynamics simulations⁴¹ were carried out with the number of molecules, the system volume, and the temperature held constant using the third-party code NAMD.⁴² The temperature was maintained at 298.15 K by applying a Langevin thermostat, with a damping coefficient of 0.5 ps^{-1} , to non-hydrogen atoms. The Verlet method was used to perform the numerical integration of the equations of motion for the monolayer while SETTLE (Ref. 43) was used for water. All bond lengths in the monolayer were kept fixed using SHAKE.⁴⁴ A timestep of 1 fs was used. The SPC/E interaction potential⁴⁵ was used for water while the OPLS-UA force field^{46,47} was used for the monolayer (see Table I). The OPLS combining rules were used for water-monolayer interactions. The interactions between atoms in the same monolayer chain separated by three or fewer bonds were excluded. Short-range interactions were cutoff at 12 \AA with a switching function applied for separations greater than 10 \AA . The dimensions of the simulation cell were $L_x=447.30 \text{ \AA}$, $L_y=34.43 \text{ \AA}$, and $L_z=173.49 \text{ \AA}$. Periodic boundary conditions in three dimensions were used. The PME technique^{48,49} was used to account for long-range interactions with the smallest number of

TABLE I. Force field for the MD simulations.

Bond	Length (Å)		
O-H ^a	1.000		
O-H	0.945		
CH ₂ -O	1.430		
CH ₂ -CH ₂	1.530		
CH ₂ -CH ₃	1.530		
Valence	k_θ	θ_0 (deg)	
H-O-H ^a	...	109.47	
H-O-CH ₂	110.02	108.5	
O-CH ₂ -CH ₂	100.09	108.0	
CH ₂ -CH ₂ -CH ₂	124.20	112.0	
CH ₂ -CH ₂ -CH ₃	124.20	112.0	
The valence potential energy is given by $U=k_\theta/2(\theta-\theta_0)^2$. k_θ is given in units of kcal/mol rad ² .			
Dihedral	V_1	V_2	V_3
H-O-CH ₂ -CH ₂	0.834	-0.116	0.747
O-CH ₂ -CH ₂ -CH ₂	0.702	-0.212	3.060
CH ₂ -CH ₂ -CH ₂ -CH ₂	1.411	-0.271	3.145
CH ₂ -CH ₂ -CH ₂ -CH ₃	1.411	-0.271	3.145
The dihedral potential energy is given by $U=V_1/2(1+\cos \phi)+V_2/2(1-\cos 2\phi)+V_3/2(1+\cos 3\phi)$. V_i are given in units of kcal/mol.			
Nonbonded i - i	σ_{ii} (Å)	ϵ_{ii}	q_i (e)
H-H ^a	0.0	0.0	0.4238
O-O ^a	3.166	650.2	-0.8476
H-H	0.0	0.0	0.265
O-O	3.070	711.8	-0.700
CH ₂ -CH ₂ ^b	3.905	493.9	0.435
CH ₂ -CH ₂ ^b	3.905	493.9	0.0
CH ₃ -CH ₃	3.905	732.5	0.0
The Lennard-Jones potential energy is given by $U=4\epsilon_{ij}[(\sigma_{ij}/r_{ij})^{12}-(\sigma_{ij}/r_{ij})^6]$. ϵ_{ij} are given in units of J/mol. The Coulomb interaction is $(4\pi\epsilon_0)^{-1}q_iq_jr_{ij}^{-1}$.			

^aThese parameters apply to SPC/E water while all others apply to the binary SAM.

^bA CH_2 united atom is neutral except when directly bonded to an alcohol group, where it has a partial charge of 0.435 e . The OPLS combining rules are $\sigma_{ij}=\sqrt{\sigma_{ii}\sigma_{jj}}$ and $\epsilon_{ij}=\sqrt{\epsilon_{ii}\epsilon_{jj}}$.

grid points per direction being 0.90 \AA^{-1} . The simulations were carried out on DataStar at the San Diego Supercomputer Center. Using 18 IBM p655 nodes or 144 processors, the simulations ran at roughly 14 ms/step.

III. RESULTS AND DISCUSSION

A. Lennard-Jones system

The Lennard-Jones droplet began as a rectangular arrangement of atoms at the low- c end of the wetting gradient. During the first 600τ of the simulation, the droplet is found to rearrange itself into a spherical-cap form [Figs. 3(a) and 3(b)] with little change in the center-of-mass position. Afterwards the drop moves continuously toward the high- c end of the strip, and its shape becomes increasingly asymmetric

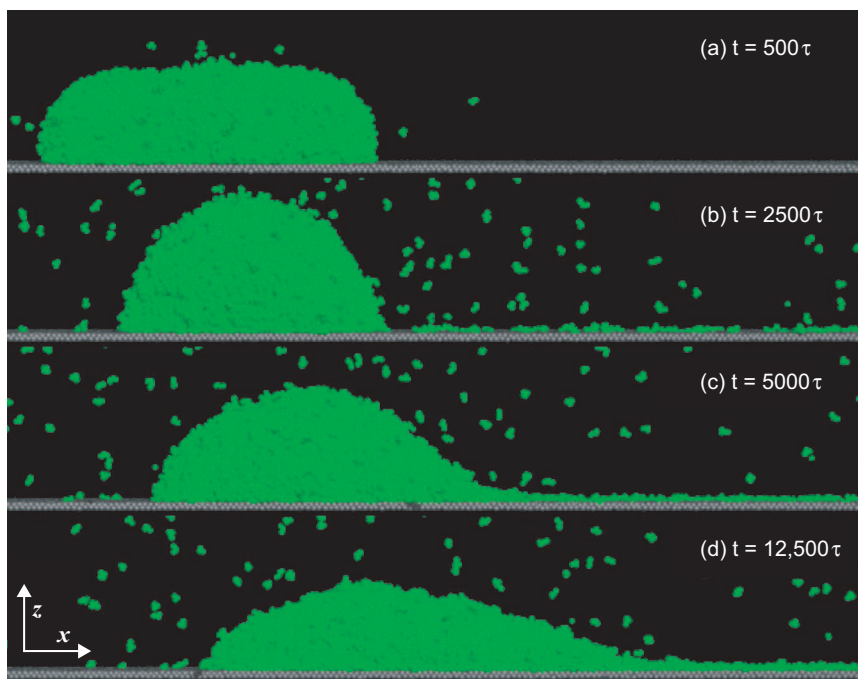


FIG. 3. (Color) Side views of a Lennard-Jones droplet at different times on a wetting gradient.

[Figs. 3(c) and 3(d)], reflecting the decrease in equilibrium contact angle along the gradient. The variation of center-of-mass position with time, shown in Fig. 4, is a simple power law after rearrangement, $x_{\text{c.m.}}(t) \sim t^n$ with $n = 0.42 \pm 0.01$. After $12.5 \times 10^4 \tau$, the center-of-mass of the droplet has moved 110σ in the x -direction. The simulation was terminated at this point since there were no qualitative changes in the drop's behavior.

The shape of the droplet is neither spherical nor cylindrical. It has a shape similar to the drops found in the molecular adsorption studies,^{16,17} which were carried out on rectilinear tracks embedded in a nonwetting background. Because of its irregular shape, the droplet does not lend itself to a simple theoretical analysis, which we therefore postpone to the second case below.

For comparison to the water drop results below, we estimate the relevant dimensionless hydrodynamic parameters describing the flow. At time 2500τ when the drop shape is very roughly a spherical cap, the radius $R \approx 40\sigma$ and the velocity $V \approx 0.015\sigma/\tau$. From Koplik *et al.*,³⁶ the fluid's density, viscosity, and surface tension are $\rho = 0.79\sigma^{-3}$, $\mu = 3.6m/(\sigma\tau)$ and $\gamma = 0.46\epsilon/\sigma^2$, respectively, where all quan-

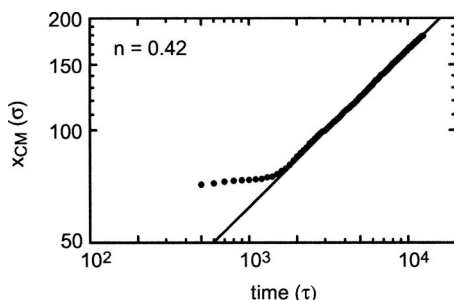


FIG. 4. A log-log plot of the axial component of the center-of-mass position vs time for a Lennard-Jones droplet on a wetting gradient. The coefficient and exponent of the power law fit are $c_{\text{LJ}} = 3.37\sigma\tau^{-0.42}$ and $n_{\text{LJ}} = 0.42$, respectively.

ties are given in units derived from the Lennard-Jones potential. The resulting Reynolds number is $\text{Re} = \rho VR/\mu \approx 2.7$, the capillary number is $\text{Ca} = \mu V/\gamma \approx 0.12$, and the Bond number is $\text{Bo} = \rho R^2 g/\sigma \approx 2 \times 10^{-10}$. The first two numbers decrease as $t^{-0.58}$ as the simulation proceeds and the drop slows.

B. Water-SAM system

The motion of water nanodroplets of different size (2000 and 4000 molecules) was investigated on nonuniform and uniform wetting gradients. The hydroxyl number density along each gradient is shown in Fig. 5. The magnitude of each gradient is the same.

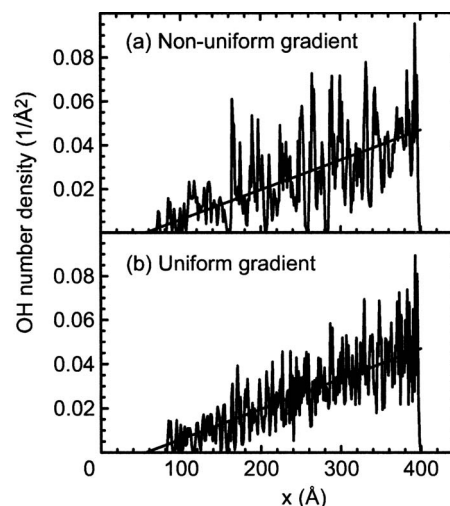


FIG. 5. The number density of hydroxyl groups as a function of position along the gradient is shown for the (a) nonuniform gradient and (b) uniform gradient. The line running through the data in both plots is the ideal or target gradient.

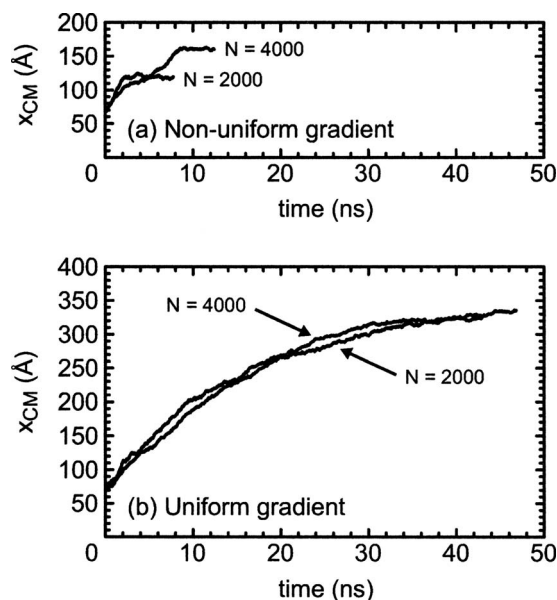


FIG. 6. The axial component of the center-of-mass position is shown for two different size water droplets on the (a) nonuniform gradient and (b) uniform gradient.

1. Nonuniform gradient

For the nonuniform case, a droplet consisting of 2000 water molecules was found to proceed along the gradient for 50 Å until the advancing edge of the droplet encountered a large patch of methyl-terminated chains at $x=160$ Å. This patch corresponds to a sharp decrease in the OH number density in Fig. 5(a). The center of mass of the nanodroplet is plotted as a function of time in Fig. 6(a). The center of mass and base length of the drop at this point were $x_{c.m.}=120$ Å and $l_b=60$ Å, respectively. After becoming pinned, the simulation was continued for an additional 4 ns. In that time, the droplet did not pass the hydrophobic patch. A second interpretation of the droplet becoming pinned is that due to the nonuniformity of the gradient the local γ_{SV} at the advancing and receding edges of the droplet were approximately the

same. In such a case, the droplet would have similar θ_a and θ_r and this would give a zero driving force as suggested by Eq. (1).

The droplet consisting of 4000 water molecules showed a similar behavior on the same nonuniform gradient. Its center of mass increased during the first 8 ns of the simulation before reaching a constant value of 160 Å for the final 4 ns. The hydrophobic patch that the droplet could not pass is located just beyond $x=200$ Å. The base length of the droplet was approximately 85 Å. In general, a larger droplet will experience a larger driving force as can be seen from Eq. (1). This might explain why the larger droplet was able to pass the hydrophobic patch at $x=160$ Å while the smaller droplet could not.

2. Uniform gradient

A second set of simulations was conducted on a uniform gradient with the same overall strength as the nonuniform gradient. Figure 5 shows that the OH number density varies more smoothly in this case. On the uniform gradient, the small and large water droplets were found to move all the way from the hydrophobic to the hydrophilic end. The axial component of the center-of-mass position is shown as a function of time in Fig. 6(b) for the two droplet sizes. It can be seen that both size droplets move with approximately the same speed. While the average center-of-mass motion of the drops is continuous, thermal fluctuations give rise to slight positive and negative local displacements.

A time sequence of configurations for the $N=2000$ water droplet on the uniform gradient is shown in Fig. 7. At $t=0$, the droplet is placed at the hydrophobic end of the gradient where the advancing and receding contact angles are both greater than 90° . At $t=7.5$ ns, the droplet has advanced about 100 Å and θ_a and θ_r have both decreased. Figure 7(c) shows a snapshot at $t=15.0$ ns where the advancing contact angle is less than the receding contact angle. This behavior is not seen in every snapshot because thermal fluctuations are large and the droplet shape is often distorted as in Fig. 7(b). However, a time average of the liquid-vapor profile, as shown in

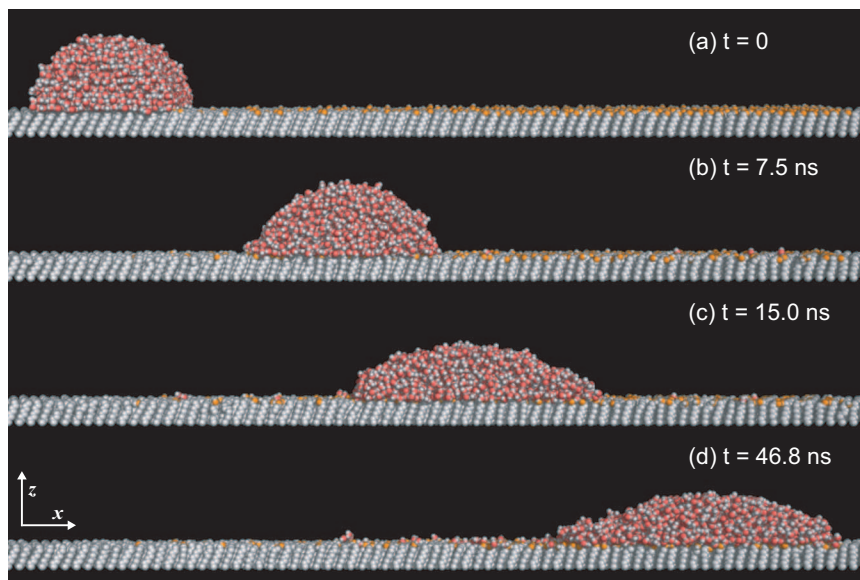


FIG. 7. (Color) Side views of the $N = 2000$ water nanodroplet at different times on a uniform wetting gradient. (a) The droplet is initialized with a hemicylindrical shape at the hydrophobic end. Intermediate configurations are shown in (b) and (c) with the final configuration in (d). The water molecules are shown with oxygen colored red and hydrogen in white, while the substrate is shown with methyl and methylene groups as gray, oxygen as orange, and hydrogen as white.

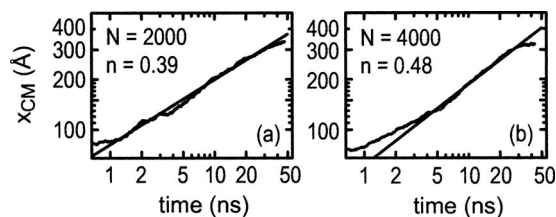


FIG. 8. The center-of-mass position vs time on a log-log plot for water droplets on a uniform wetting gradient with (a) $N=2000$ and (b) $N=4000$ molecules per drop. The lines are the power law fits to the data between 5 and 35 ns.

Fig. 9(a), reveals that θ_a is indeed less than θ_r in Fig. 7(b). It can also be seen that the base length of the ridge broadens with time. The droplet traverses the gradient in roughly 45 ns. The number density of hydroxyl groups goes abruptly to zero at the end of the hydrophilic region. This explains why the droplet has a larger contact angle at the front rather than the rear in the last snapshot of the sequence.

To evaluate the relative importance of different forces we compute various dimensionless groups using the following values: $\gamma=72$ mN/m, $\mu=1$ mPa s, $\rho=10^3$ kg/m³, $g=9.8$ m/s², $V=1$ m/s, and $R=10^{-8}$ m. The capillary number is $Ca \approx 10^{-2}$. The Bond number is $Bo \approx 10^{-11}$. The small values of the Ca and Bo number suggest that gravity is unimportant and that the droplet shape is dominated by surface forces and not the motion. This analysis does not account for the role of thermal fluctuations. The Reynolds number is $Re \approx 10^{-2}$. The small value of Re justifies the use of the Stokes equations as the starting point for the derivation of the drag force.

As was done for the Lennard–Jones case, we fit the center-of-mass position data to a simple power law, $x_{c.m.} = ct^n$, for the uniform gradient cases. These data are shown on a log-log plot in Fig. 8. The values of n have been determined to be 0.39 and 0.48 for the small and large droplets, respectively, with the coefficients being $c=81.6$ Å ns^{-0.39} and

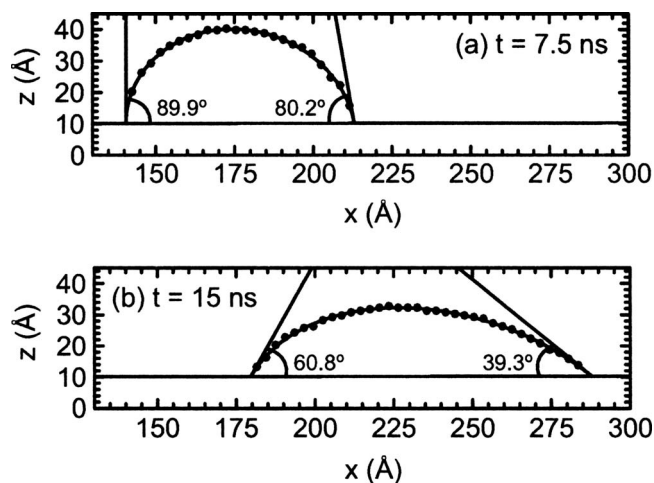


FIG. 9. Best-fit ellipses to the liquid-vapor boundary profile data at (a) $t=7.5$ ns and (b) $t=15.0$ ns for the $N=2000$ water droplet on a uniform wetting gradient. The horizontal line at approximately $z=10$ Å is the total height of the monolayer which increases gently in the positive x -direction. The bottom layer of fixed atoms is located at $z=0$. The tangent lines at the advancing and receding edges of the drop are shown.

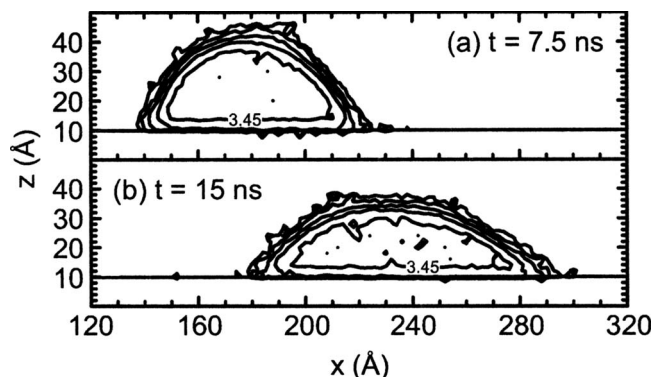


FIG. 10. Contours of average number of hydrogen bonds per water molecule are shown. The contours are 3.45, 3.15, 2.85, 2.55, and 2.25 in going from the bulk to the surface. The time-averaged liquid-vapor profile of each droplet is roughly between the 3.15 and 2.85 contours.

61.6 Å ns^{-0.48}. For the Lennard–Jones simulation, we found $n=0.42$ (see Fig. 4). Despite the many differences between the Lennard–Jones and water-SAM systems such as the presence of long-range forces and hydrogen bonding in the water-SAM case, the two systems exhibit a similar overall behavior for the motion.

To determine the shape of the droplet at time t , the time-averaged fluid density field is found. Space is divided into nonoverlapping rectangular slabs with dimensions $\Delta x=3.0$ Å, $\Delta y=L_y$, and $\Delta z=0.5$ Å. Water molecules from each configuration are individually assigned to a slab based on their center-of-mass positions. Once the density field has been calculated for a given time interval, the vapor-liquid boundary is found by determining the position of the first bin in the z -direction for each x -slab where the water density falls to one-half of its bulk value. The data points $\{x_i, z_i\}$ are then fitted to an ellipse⁵¹ using a nonlinear fitting routine. The contact angles, positions of the edges, and base length are then straightforwardly determined. Figure 9 shows the profile data points and the best-fit ellipse at $t=7.5$ ns and 15 ns for the small droplet.

Because the droplet is constantly moving down the gradient care must be taken in performing the time average. Figure 6(b) suggests that the maximum velocity of either size droplet is roughly 50 Å/ns or 0.05 Å/ps. In finding the profile at time t , we consider configurations from $t \pm 100$ ps in the averaging. This gives a worst case scenario difference in $x_{c.m.}$ of (100 ps) (0.05 Å/ps)=5 Å in each direction. For most profiles, the difference is closer to 1 Å. In an attempt to remove the small effect of droplet translation from the average, the center of mass of each configuration is shifted to that at time t . Since configurations are stored every 5 ps, a total of 41 configurations are considered per profile.

The height of the monolayer increases slightly in the direction of increasing hydroxyl concentration. Methyl-terminated chains are found to give a total monolayer height of 10.03 Å while alcohol-terminated chains give 10.41 Å. Because the determination of the contact angle is a sensitive measurement, the change in height is taken into account by assuming that it varies linearly between the two ends.

It can be seen from Fig. 7(d) that a small number of molecules have detached from the droplet and assumed po-

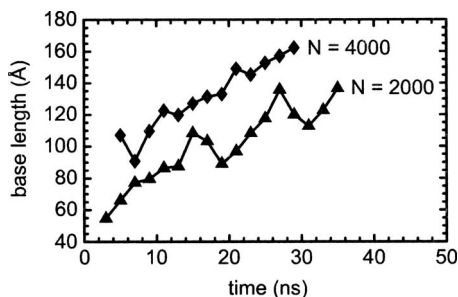


FIG. 11. The base length of a cylindrical-cap water droplet on a uniform wetting gradient as a function of time. The lines are drawn to guide the eye.

sitions in the intermediate region of the gradient. These water molecules hydrogen bond with each other and the hydroxyl-terminated chains in the monolayer. Since these molecules have fewer hydrogen bonds on average than the molecules in the main droplet, it is expected that many will recombine with the main droplet at later times. A contour plot illustrating the average number of hydrogen bonds per water molecule is shown in Fig. 10. This plot was constructed using the averaging procedure described above with $\Delta x = 2.0$ Å and $\Delta z = 2.0$ Å and the geometric hydrogen-bonding criteria of Martí.⁵⁰ For both droplets, the average number of hydrogen bonds per water molecule in the bulk is found to be 3.45–3.55, which is in agreement with the range of Daub *et al.*⁵¹ of 3.48–3.51. It can be seen from Fig. 10(a) that there are more hydrogen bonds formed between the droplet and the monolayer in the advancing half of the droplet. At $t = 7.5$ ns, the number of hydrogen bonds in the z -slab between 8–10 Å is found to vary from 2.81 at $x = 150$ Å to 3.14 at $x = 210$ Å. At $t = 15$ ns, this value varies from 2.95 at $x = 190$ Å to 3.25 at $x = 280$ Å.

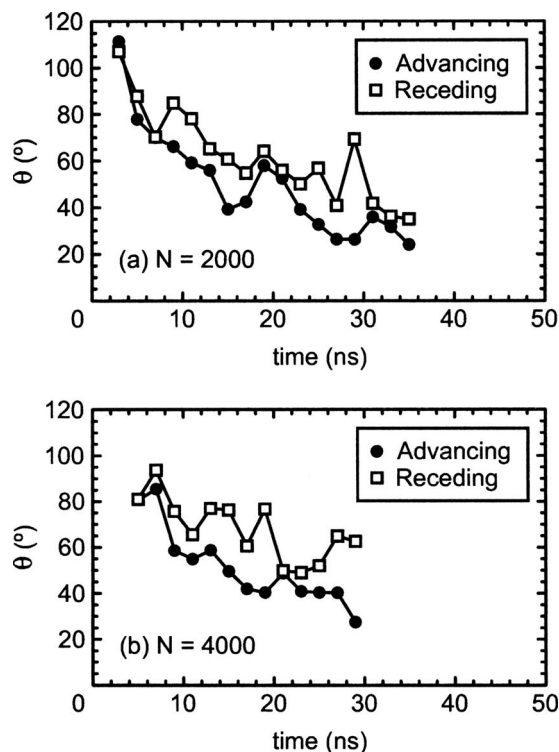


FIG. 12. Advancing and receding contact angles as a function of time for (a) $N = 2000$ and (b) $N = 4000$ water molecules per drop. The lines are drawn to guide the eye.

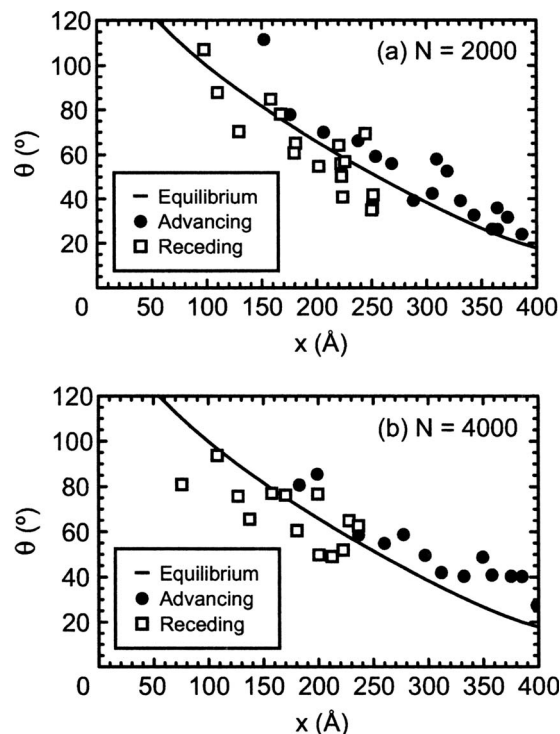


FIG. 13. Advancing and receding contact angles as a function of position along the gradient for the (a) $N = 2000$ and (b) $N = 4000$ water molecule droplet. The angles were measured by fitting each time-averaged droplet profile to an ellipse. The data were calculated for the smaller droplet every 2 ns from 3 to 35 ns and for the larger droplet every 2 ns from 5 to 29 ns. $\theta_e(x)$ is given by the solid curve.

Figure 11 shows the base length of the droplets as a function of time. The base length is defined as the difference between the positions of the advancing and receding edges. The base length increases with time because at greater axial positions, the droplet interacts with a substrate having an effectively higher γ_{SV} . Greater variability is seen for the $N = 2000$ water droplet. Its base length undergoes two contractions with the first terminating at $t = 19$ ns and the second at $t = 31$ ns. The contraction between 15 and 19 ns is due to the advancing edge becoming slowed by a region of elevated hydrophobicity at $x = 305$ Å. During this time period, the receding edge increases by 40.6 Å while the advancing edge by only 21.2 Å. Figure 12 shows the advancing and receding contact angles as a function of time for both droplet sizes. The difference between θ_a and θ_r at $t = 19$ ns is only 6.2° , whereas at $t = 15$ ns it is 21.5° . The second dramatic reduction of the base length is due to a series of events occurring between 19 and 31 ns. From 19 to 27 ns the receding edge of the droplet is pinned at $x = 222$ Å. During this period, the advancing edge increases by 50.3 Å which leads to a rapid increase in the base length. The advancing edge then becomes pinned from 27 to 31 ns at $x = 365$ Å, while the receding edge passes the hydrophobic patch at $x = 222$ Å and increases by 27.7 Å. This explanation is consistent with the behavior of the dynamic contact angles shown in Fig. 12. The receding edge then becomes pinned at $x = 250$ Å between 31 and 35 ns. The base length of the larger droplet is seen to increase much more steadily. This might be explained by the increased driving force.

The measurements of the advancing and receding contact angles were made every 2 ns. Figure 12 indicates that, in general, θ_a is less than θ_r at t . The average difference between the cosine of the advancing and receding angles (i.e., $\cos \theta_a - \cos \theta_r$) is 0.18 for the smaller droplet and 0.24 for the larger droplet. This is expected since the larger droplet has a larger base length and therefore its leading and rear edges experience a greater difference in the hydroxyl surface concentration.

Several authors have shown that contact angle hysteresis plays an important role in determining the motion of the droplet.^{4,7,9,15} Hysteresis in the contact angle may be probed by examining θ_a and θ_r as a function of position along the gradient. On an ideal surface, the advancing and receding contact angles are the same at all locations. Figure 13 shows θ_a and θ_r as a function of position for the two droplet sizes. The solid curve in the figure gives the equilibrium contact angle θ_e , which was taken from our previous work.³⁴ In general, we find $\theta_r(x) < \theta_e(x) < \theta_a(x)$, which indicates the presence of contact angle hysteresis. It is difficult to be precise about the extent of hysteresis because of the scatter in the data. Since the measurements were made uniformly in time, clusters of overlapping symbols are indicative of pinning. For θ_r this occurs at $x=222$ and 250 Å and for θ_a this occurs at $x=365$ Å. These observations are consistent with the data in Figs. 11 and 12.

For macroscopic systems, hysteresis in the contact angle is commonly caused by contaminants, substrate roughness, or a substrate that is chemically heterogeneous. Since contaminants are not present in the molecular systems considered here, the origin of hysteresis must be related to the fluid-substrate interaction. The NN separation distance in the monolayer is 4.97 Å, while the length of an OH bond in water is only 1 Å. The droplet edge which is composed of only tens of water molecules sees the SAM as chemically and topologically heterogeneous. As Fig. 5 indicates, the surface concentration of the hydroxyl-terminated chains (which are arranged nonuniformly in both the x - and y -directions) only appears to follow the target value of the gradient when averaged over several nanometers. This has important consequences when the advancing and receding contact angles are measured at the same location on the gradient. With reference to Fig. 1, when θ_a is measured at position x_0 , the droplet is at lesser x while for the measurement of θ_r at the same position the droplet is at greater x . Because of this the droplet edges at x_0 see different regions of the substrate and this leads to a different balance of forces at the contact line or a different contact angle. If the simulations were conducted with the substrate modeled as a continuum, it is expected that the extent of hysteresis would be greatly reduced if not eliminated. Lastly, since Ca is small the hysteresis is more of a result of the heterogeneous nature of the substrate than the motion of the droplet.

3. Comparison to theory

The simulations give the center-of-mass position of the droplet as a function of time or the velocity. We now compare the velocity gotten by simulation with that predicted by theory.

The data in Fig. 6(b) have been fitted to a power law or $x_{c.m.} = ct^n$. The velocity is then $V = nct^{n-1}$ or

$$V = nc^{1/n} x_{c.m.}^{1-1/n}. \quad (5)$$

The quasisteady velocity of a ridge on a wetting gradient has been estimated by Brochard.³ By equating the driving force [Eq. (1)] and the drag force [Eq. (2)] the velocity is found to be

$$V = \frac{\gamma[\cos \theta_e(x_a) - \cos \theta_e(x_r)]\theta_0}{6\mu \ln(x_{\max}/x_{\min})}. \quad (6)$$

The value of x_{\min} must be estimated before Eq. (6) can be evaluated. The results of nonequilibrium molecular dynamics simulations by Thompson *et al.*⁵² suggest that $x_{\min} \approx 1.8\sigma$ for simple fluid-solid systems. Using this recommendation with $\sigma = \sigma_{OO}$, we find $x_{\min} \approx 5.7$ Å. The values of x_{\max} can be estimated from Fig. 11. For the $N=2000$ droplet, one-half the base length varies from 27.4 to 64.4 Å. This means that the ratio x_{\max}/x_{\min} varies from roughly 5 to 11. For the larger droplet, the slip length is taken to be the same and this leads to the ratio varying from 8 to 14.

One concern in applying Eq. (1) to describe the driving force is that it does not account for contact angle hysteresis. The expression was derived for ideal surfaces and when applied to real surfaces it overpredicts the force. If knowledge of the advancing and receding contact angles is available, then those values can be used in place of the equilibrium angles appearing in Eq. (1). Approaches to modify the driving force for spherical droplets have been described.^{9,15} Second, given that the driving force depends on $\theta_e(x)$, one must question how well contact angles are reproduced by molecular droplets. This concern has been addressed by Hautman and Klein⁵³ who pointed out that the contact angle of a sessile drop may be calculated accurately as long as the bulk region of the droplet is sufficiently large (i.e., the height of the drop is greater than the sum of the liquid-vapor and solid-liquid interfacial thicknesses). These criteria are satisfied for droplets of water on SAMs consisting of as few as 90 molecules. Additional simulation studies have also found good agreement between the microscopic and macroscopic contact angles.^{34,54,55} Third, since the curvature of a cylindrical cap in the plane of the substrate is infinite, the line tension makes no contribution to the force balance at the three-phase contact line. This is not true for small spherical-cap droplets where the line tension may play a significant role in determining the droplet profile. Last, the liquid-vapor tension appears in Eq. (1). The SPC/E model of water at 300 K has been reported to have a surface tension of 55.4 ± 3 mN/m, which is 23% lower than the experimental value of 71.7 mN/m.⁵⁶ If the value of 55.4 mN/m holds for the droplets in our simulations, then this would have the effect of lowering the driving force.

The derivation of the hydrodynamic drag force $F^{(h)}$ is based on lubrication theory which assumes that the height of the droplet is much less than the base length or, equivalently, that the contact angle is small. At the beginning of the simulations, both the advancing and receding contact angles are greater than 90° suggesting immediately that the derivation makes assumptions that are violated. When Moumen *et al.*¹⁵

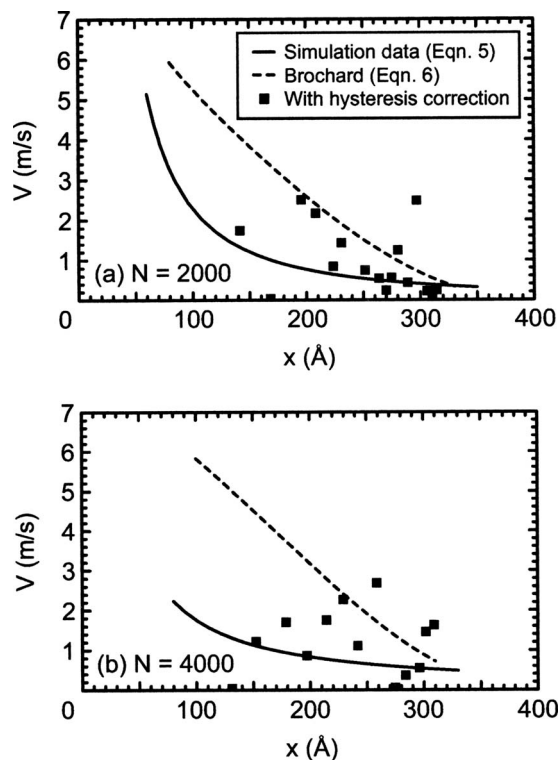


FIG. 14. Droplet velocity as a function of position along the gradient as gotten by simulation and theory for (a) $N=2000$ and (b) $N=4000$ water molecules per drop. Edge effects are taken into account by only considering velocities on the intermediate region of the gradient.

used their expression for the hydrodynamic force, which is based on lubrication theory, to compare the droplet velocity to experimental data they found increasing agreement with increasing position along the gradient where the contact angle is smaller. Additional simplifications in the derivation of Eq. (2) include the expansion of trigonometric functions of the contact angle to first order and the assumption that the droplet profile may be treated as a pair of wedges with equal wedge angles. This latter approximation is valid for small gradient strengths but droplet profiles from the simulations are seen to be asymmetric (Fig. 9) indicating a relatively strong gradient in the present work. The fluid property appearing in Eq. (2) is the viscosity. At 301 K, the viscosity of the SPC/E model is reported to be 0.91 mPa s,⁵⁷ which agrees well with the experimental value of 0.85 mPa s.

Before plotting Eq. (6), the best-fit line to the simulation results of the base length versus center-of-mass position was found for each drop size. Using this least squares approximation, the value of x_{\max} for a given x was found as one-half the base length. The advancing/receding edge position of the droplet was assumed to be found by adding/subtracting half the base length from the center-of-mass position. The cosine of the equilibrium water contact angle at the advancing and receding edges were gotten by evaluating a second-order interpolating polynomial: $a_2\chi_p^2 + a_1\chi_p + a_0$ with $a_2 = -1.64$, $a_1 = 3.10$, and $a_0 = -0.497$, where χ_p is the local mole fraction of HOCH₂-terminated chains. The interpolating polynomial is based on simulation data from a previous study³⁴ of uniformly mixed monolayers.

Figure 14 compares the simulation results with the the-

oretical predictions for the quasisteady velocity of the droplet. The simulation results [Eq. (5)] are given by the solid curve while Brochard's solution [Eq. (6)] is drawn as a dashed curve. The predicted velocity is found to overestimate the measured values at all positions and for both droplet sizes. Better agreement is seen for the smaller droplet. Brochard's prediction is nearly linear with a slight change in slope toward the end of the gradient. The simulations show the velocity to decrease rapidly for small and intermediate values of the axial coordinate and then only slightly for large values. Moumen *et al.*¹⁵ experimentally measured the droplet velocity as a function of position along the gradient. Because the water contact angle in their case is approximately constant over the first 2.5 mm of the gradient, a maximum is seen in the velocity as a function of position. However, beyond the position where the maximum occurs, the experimental results appear to follow a power law. In the present work, the water contact angle varies smoothly with position (see Fig. 13) so no maximum is seen. This suggests that the qualitative difference between the two curves in Fig. 14 arises from simplifications made in the derivation of Eq. (6). Note that for both droplet sizes the agreement becomes better as the dynamic contact angle decreases, which is when the lubrication approximation becomes more justified.

Despite the many assumptions in the derivation of Eq. (6), the agreement between the simulation results and the theoretical predictions is fair. Because contact angle hysteresis is ignored in Eq. (6), the theory gives higher velocities than those found by simulation. One simple way to account for the effect of hysteresis is to use the advancing and receding contact angles instead of the equilibrium values. With this modification, the driving force becomes

$$F^{(Y)} = \gamma[\cos \theta_a(x_a) - \cos \theta_r(x_r)]. \quad (7)$$

The square symbols in Fig. 14 give the velocity of the droplet when the driving force is based on the measured values of $\theta_a(x_a)$ and $\theta_r(x_r)$. While the data with the hysteresis correction are scattered, in general, better agreement is seen.

The small and large droplets were found to move with approximately the same speed. For the same center-of-mass position, the ratio of the base length of the larger droplet to that of the smaller droplet decreases from 1.6 to 1.3 as $x_{c.m.}$ increases. According to Eq. (6), if we assume that the cosine of the equilibrium contact angle varies linearly with position and the droplet profile is circular, then

$$V \sim \frac{l_b}{\ln(l_b/s)}, \quad (8)$$

where $s = 2x_{\min}$. Using the base length data from the simulations, Eq. (8) suggests that the speed of the larger droplet should be 1.2 to 1.3 times faster than the smaller droplet. This factor is not very large and might be offset by the effect of contact angle hysteresis. For a spherical-cap droplet on a wetting gradient, the speed is found to be proportional to the base radius of the droplet.

Figure 14 indicates that the water nanodroplets move with speeds of m/s. The numerous millimeter-scale experimental studies on spherical-cap droplets typically report ve-

locities of mm/s. Thus, an increase in speed of three orders of magnitude is found in going from the millimeter to the nanometer scale.

A cylindrical fluid droplet is unstable and will break up into spherical-cap droplets with time.⁵⁸ Our simulations enforce stability by the small choice of the width of the simulation cell. Spherical nanodroplets were not considered in this work because even on a one-dimensional gradient the droplet would spread significantly in two dimensions. Because of this, the simulation cell would have to be increased in the y -direction to ensure that image droplets do not influence the results. A significant amount of CPU time above that for the cylindrical droplet case would be needed to simulate spherical droplets.

C. Approximate argument for the velocity

An approximate calculation of the motion of a liquid ridge on a wettability *step* has been given by Ondarçuhu and Raphaël,⁵⁹ based on the type of simplifying assumptions often utilized by de Gennes.¹ Here we extend these methods to calculate the velocity of a ridge in a wettability gradient.

The starting point is an expression for the velocity of a moving contact line in the “wedge” limit, where the dynamic contact angle is assumed to be small so that the lubrication approximation may be used for the flow field within the liquid. In this case, de Gennes⁶⁰ argues that the contact line velocity is

$$V = \frac{k\gamma}{\mu} \theta (\theta^2 - \theta_e^2), \quad (9)$$

where γ and μ are the liquid-vapor surface tension and the fluid viscosity, respectively, θ_e is the equilibrium contact angle, θ is the dynamic contact angle, and k is a numerical coefficient. The formula may be understood by regarding the factor $\gamma(\theta^2 - \theta_e^2) \approx \gamma(\cos \theta_e - \cos \theta)$ as representing the unbalanced surface tension force at the contact line and $\mu/k\theta$ as an effective viscous drag coefficient, although the original argument is in terms of flow dissipation. For a ridge, Ondarçuhu and Raphaël employed this formula separately for the advancing and receding contact angles at the front and rear, and made the further approximation that in slow flows the pressure equalizes within the ridge, which then has constant curvature and therefore *equal* dynamic contact angles on both sides. The latter assumption is not entirely correct and indeed this behavior is not seen in our numerical simulations, but it is difficult to devise another approximation for the shape of the ridge which would specify the relation between advancing and receding angles. The liquid ridge changes position in their case because the ridge straddles a step in wettability, so that the equilibrium contact angles differ on the two sides, which then have different velocities.

In the case of a uniform wettability gradient (Fig. 1), the solid-liquid surface tension and therefore $\cos \theta_e$ increase linearly in the direction (x) of mean flow, so we assume that the driving force at each contact line is a linear function of position. With an appropriate choice of origin, we write $\gamma(\cos \theta - \cos \theta_e) = \alpha x$, where $\alpha > 0$ is proportional to the sur-

face tension gradient. Applying this reasoning to a ridge with advancing and receding edges at $x_{1,2}$, respectively, from Eq. (9) we have

$$\dot{x}_i = v_0 \theta x_i, \quad i = 1, 2 \quad (10)$$

where $v_0 = k\alpha/\mu$ and θ is the common contact angle. The positions of the edges are constrained by the constant volume of liquid, which in the wedge approximation requires

$$(x_1 - x_2)^2 \theta = \text{const.} \quad (11)$$

Differentiating this expression with respect to time and substituting $\dot{x}_{1,2}$ from the previous one yield

$$2v_0\theta^2 + \dot{\theta} = 0 \quad \text{so} \quad \theta(t) = \frac{\theta_0}{1 + 2v_0\theta_0 t}, \quad (12)$$

and from Eq. (10) we find

$$x_i(t) = x_i(0)(1 + 2v_0\theta_0 t)^{1/2}. \quad (13)$$

Therefore, both the mean position $[x_1(t) + x_2(t)]/2$ and the width of the ridge $[x_1(t) - x_2(t)]$ increase as $t^{1/2}$ within this approximation, while the contact angle decreases as $\theta(t) \sim 1/t$. The simulations can be fitted to power laws with exponents that are similar but not identical, but given the severe nature of the approximation made, we regard the calculation as qualitatively consistent with the numerical results.

IV. CONCLUSIONS

Molecular dynamics simulations of Lennard-Jones and water nanodroplets were conducted to investigate the motion of a liquid droplet on a wetting gradient. The two different systems exhibited a similar overall behavior for the motion with a simple power law describing the center-of-mass position with time. For the water nanodroplets, the uniformity of the gradient was found to be an important factor in determining whether the droplet traversed the entire gradient or became pinned at an intermediate position. These simulations have demonstrated the ability of wetting gradients to move nanodroplets of water over distances of tens of nanometers or nearly ten times the initial base radius of the droplet. Fair agreement was seen between the simulation results for the droplet velocity and the theoretical predictions. When contact angle hysteresis was accounted for by basing the driving force on the measured advancing and receding contact angles instead of the equilibrium values the agreement was found to improve.

ACKNOWLEDGMENTS

This work was funded by a NSF IGERT Graduate Research Fellowship in Multiscale Phenomena of Soft Materials, and it was supported in part by the National Science Foundation through a large resource allocation (LRAC) on DataStar at the San Diego Supercomputer Center. We thank M. Rauscher for bringing Ref. 59 to our attention.

¹P. G. de Gennes, *Rev. Mod. Phys.* **57**, 827 (1985).

²H. P. Greenspan, *J. Fluid Mech.* **84**, 125 (1978).

³F. Brochard, *Langmuir* **5**, 432 (1989).

⁴M. K. Chaudhury and G. M. Whitesides, *Science* **256**, 1539 (1992).

⁵H. Elwing, S. Welin, A. Askendal, U. Nilsson, and I. Lundstrom, *J.*

- Colloid Interface Sci.* **119**, 203 (1987).
- ⁶M. L. Ford and A. Nadim, *Phys. Fluids* **6**, 3183 (1994).
 - ⁷S. Daniel, M. K. Chaudhury, and J. C. Chen, *Science* **291**, 633 (2001).
 - ⁸K. Ichimura, S. Oh, and M. Nakagawa, *Science* **288**, 1624 (2000).
 - ⁹S. Daniel and M. K. Chaudhury, *Langmuir* **18**, 3404 (2002).
 - ¹⁰S. Daniel, S. Sircar, J. Gliem, and M. K. Chaudhury, *Langmuir* **20**, 4085 (2004).
 - ¹¹H. Suda and S. Yamada, *Langmuir* **19**, 529 (2003).
 - ¹²Y. Ito, M. Heydari, A. Hashimoto, T. Konno, A. Hirasawa, S. Hori, K. Kurita, and A. Nakajima, *Langmuir* **23**, 1845 (2007).
 - ¹³R. S. Subramanian, N. Moumen, and J. B. McLaughlin, *Langmuir* **21**, 11844 (2005).
 - ¹⁴R. G. Cox, *J. Fluid Mech.* **168**, 169 (1986).
 - ¹⁵N. Moumen, R. Shankar Subramanian, and J. B. McLaughlin, *Langmuir* **22**, 2682 (2006).
 - ¹⁶F. D. Dos Santos and T. Ondarçuhu, *Phys. Rev. Lett.* **75**, 2972 (1995).
 - ¹⁷S. Lee and P. Laibinis, *J. Am. Chem. Soc.* **122**, 5395 (2000).
 - ¹⁸G. C. H. Mo, W. Y. Liu, and D. Y. Kwok, *Langmuir* **21**, 5777 (2005).
 - ¹⁹J. Zhang and Y. Han, *Langmuir* **23**, 6136 (2007).
 - ²⁰G. M. Whitesides and P. E. Laibinis, *Langmuir* **6**, 87 (1990).
 - ²¹L. Dubois and R. Nuzzo, *Annu. Rev. Phys. Chem.* **43**, 437 (1992).
 - ²²F. Schreiber, *Prog. Surf. Sci.* **65**, 151 (2000).
 - ²³C. Vericat, M. E. Vela, G. A. Benitez, J. A. Martin Gago, X. Torrelles, and R. C. Salvarezza, *J. Phys.: Condens. Matter* **18**, 867 (2006).
 - ²⁴C. E. D. Chidsey and D. N. Loiacono, *Langmuir* **6**, 682 (1990).
 - ²⁵N. Camillone, C. E. D. Chidsey, G. Liu, and G. J. Scoles, *Chem. Phys.* **98**, 3503 (1993).
 - ²⁶G. E. Poirier, *Chem. Rev. (Washington, D.C.)* **97**, 1117 (1997).
 - ²⁷X. Torrelles, C. Vericat, M. Vela, M. H. Fonticelli, M. Millone, R. Felici, T. Lee, J. Zegenhagen, G. Munoz, J. A. Martin-Gago, and R. C. Salvarezza, *J. Phys. Chem. B* **110**, 5586 (2006).
 - ²⁸A. Ripoan and G. Liu, *J. Phys. Chem. B* **110**, 23926 (2006).
 - ²⁹T. Li, I. Chao, and Y. Tao, *J. Phys. Chem. B* **102**, 2935 (1998).
 - ³⁰M. H. Adao, M. de Ruijter, M. Voué, and J. De Coninck, *Phys. Rev. E* **59**, 746 (1999).
 - ³¹M. Lundgren, N. L. Allen, and T. Cosgrove, *Langmuir* **23**, 1187 (2007).
 - ³²A. Dupuis and J. M. Yeomans, *Int. J. Numer. Methods Fluids* **50**, 255 (2006).
 - ³³G. S. Grest, D. R. Heine, and E. B. Webb, *Langmuir* **22**, 4745 (2006).
 - ³⁴J. D. Halverson, J. Koplik, A. Couzis, and C. Maldarelli (unpublished).
 - ³⁵K. Kremer and G. S. Grest, *J. Chem. Phys.* **92**, 5057 (1990).
 - ³⁶J. Koplik, T.-S. Lo, M. Rauscher, and S. Dietrich, *Phys. Fluids* **18**, 031104 (2006).
 - ³⁷C. D. Bain, J. Evall, and G. M. Whitesides, *J. Am. Chem. Soc.* **111**, 7155 (1989).
 - ³⁸S. R. Holmes-Farley, C. D. Bain, and G. M. Whitesides, *Langmuir* **4**, 921 (1988).
 - ³⁹M. Sprik, E. Delamarche, B. Michel, U. Rothlisberger, M. L. Klein, H. Wolf, and H. Ringsdorf, *Langmuir* **10**, 4116 (1994).
 - ⁴⁰O. Dannenberger, K. Weiss, H.-J. Himmel, B. Jager, M. Buck, and C. Woll, *Thin Solid Films* **307**, 183 (1997).
 - ⁴¹D. Frenkel and B. Smit, *Understanding Molecular Simulation*, 2nd ed. (Academic, London, 2002).
 - ⁴²J. C. Phillips, R. Braun, W. Wang, J. Gumbart, E. Tajkhorshid, E. Villa, C. Chipot, R. D. Skeel, L. Kale, and K. Schulten, *J. Comput. Chem.* **26**, 1781 (2005).
 - ⁴³S. Miyamoto and P. A. Kollman, *J. Comput. Chem.* **13**, 952 (1992).
 - ⁴⁴J. P. Ryckaert, G. Ciccotti, and H. J. C. Berendsen, *J. Comput. Phys.* **23**, 327 (1977).
 - ⁴⁵H. J. C. Berendsen, J. R. Grigera, and T. P. Straatsma, *J. Phys. Chem.* **91**, 6269 (1987).
 - ⁴⁶W. L. Jorgensen, *J. Phys. Chem.* **90**, 1276 (1986).
 - ⁴⁷W. L. Jorgensen, J. D. Madura, and C. J. Swenson, *J. Am. Chem. Soc.* **106**, 6638 (1984).
 - ⁴⁸T. A. Darden, D. M. York, and L. G. Pederson, *J. Chem. Phys.* **98**, 10089 (1993).
 - ⁴⁹U. Essmann, L. Perera, M. L. Berkowitz, T. Darden, H. Lee, and L. Pederson, *J. Chem. Phys.* **103**, 8577 (1995).
 - ⁵⁰J. Martí, *J. Chem. Phys.* **110**, 6876 (1999).
 - ⁵¹C. D. Daub, D. Bratko, K. Levung, A. Luzar, *J. Phys. Chem. C* **111**, 505 (2007).
 - ⁵²P. A. Thompson, W. B. Brinckerhoff, and M. O. Robbins, *J. Adhes. Sci. Technol.* **7**, 535 (1993).
 - ⁵³J. Hautman and M. L. Klein, *Phys. Rev. Lett.* **67**, 1763 (1991).
 - ⁵⁴M. Lundgren, N. L. Allen, T. Cosgrove, and N. George, *Langmuir* **18**, 10462 (2002).
 - ⁵⁵C. F. Fan and T. Cagin, *J. Chem. Phys.* **103**, 9053 (1995).
 - ⁵⁶A. E. Ismail, G. S. Grest, and M. J. Stevens, *J. Chem. Phys.* **125**, 014702 (2006).
 - ⁵⁷A. Glättli, X. Daura, and W. F. van Gunsteren, *J. Chem. Phys.* **116**, 9811 (2002).
 - ⁵⁸K. Sekimoto, R. Oguma, and K. Kawaski, *Ann. Phys. (N.Y.)* **176**, 359 (1987).
 - ⁵⁹T. Ondarçuhu and E. Raphaël, *Acad. Sci., Paris, C. R.* **314**, 453 (1992).
 - ⁶⁰P. G. de Gennes, *Colloid Polym. Sci.* **264**, 463 (1986).

A molecular dynamics study of the motion of a nanodroplet of pure liquid on a wetting gradient

Jonathan D. Halverson, Charles Maldarelli, Alexander Couzis, and Joel Koplik

Citation: *J. Chem. Phys.* **129**, 164708 (2008); doi: 10.1063/1.2996503

View online: <http://dx.doi.org/10.1063/1.2996503>

View Table of Contents: <http://jcp.aip.org/resource/1/JCPSA6/v129/i16>

Published by the [American Institute of Physics](#).

Additional information on J. Chem. Phys.

Journal Homepage: <http://jcp.aip.org/>

Journal Information: http://jcp.aip.org/about/about_the_journal

Top downloads: http://jcp.aip.org/features/most_downloaded

Information for Authors: <http://jcp.aip.org/authors>

ADVERTISEMENT



AIPAdvances

Submit Now

Explore AIP's new open-access journal

- Article-level metrics now available
- Join the conversation! Rate & comment on articles